Biomedical Signal Processing and Control 120 (2026) 110018

Contents lists available at ScienceDirect

Biomedical Signal Processing and Control

journal homepage: www.elsevier.com/locate/bspc

Assessment and characterization of the impact of pulmonary pathology on flow-induced acoustics using computational fluid dynamics

Khanyisani Mhlangano Makhanya [a], Muaaz Bhamjee [a,b,*], Neil Martinson [c,d], Simon Connell [a]

[a] Department of Mechanical Engineering Science, University of Johannesburg, Auckland Park, Johannesburg, South Africa
[b] Clean Energy Research Group, Department of Mechanical and Aeronautical Engineering, University of Pretoria, Lynnwood Road, Hatfield, 0028, Pretoria, South Africa
[c] Perinatal HIV Research Unit, Chris Hani Baragwanath Academic Hospital, Faculty of Health Sciences, University of the Witwatersrand, South Africa
[d] Johns Hopkins University Center for TB Research, Baltimore, MD, United States of America

ARTICLE INFO

Keywords:
Computational fluid dynamics
CFD
Exhalation
Fluid-flow
Pulmonary disease
Sound pressure level
Vocalization
Aero-acoustics

ABSTRACT

Respiratory illness is one of the major contributors to disease and disability worldwide. Assessing these conditions typically involves in-person evaluations at primary care or hospitals, which can be difficult to access in under-resourced areas, or during pandemics. This study explores a novel approach to assess pulmonary disease by analysing changes in cough acoustics. We posit that vocalization may provide insights into an underlying lung pathology. Utilizing computational fluid dynamics, this study investigates flow-induced changes to vocalization, cough, and lung-generated acoustics for diagnosing pulmonary pathology. We use pneumonia, bronchiectasis, and cavitary tuberculosis as exemplars. A computational fluid dynamics model was developed to simulate the acoustic properties of both healthy and diseased lungs, and validated using data from 22 vocal recordings of infected patients with distinct clinical diagnoses. The study employed two computational fluid dynamics methods: Large Eddy Simulation (LES) with the Ffowcs Williams and Hawkings model and the Realizable $k-\epsilon$ model with the Broadband Noise Source Model. Our models suggest differences in sound pressure levels across a frequency range of 0 kHz to 16 kHz, with healthy lungs exhibiting higher sound pressure levels compared to those affected by the other conditions. Comparative analysis between actual cough recordings and our model predictions indicate qualitative correlations, suggesting that our model could enhance the understanding of flow-induced acoustics in various lung pathologies. The results suggest potential for developing synthetic datasets to train artificial intelligence models aimed at telemedicine-based diagnosis, thereby improving access to initial respiratory assessments and triage.

1. Introduction

Respiratory diseases impose a significant strain on individuals, communities, and governments. In South Africa, tuberculosis (TB) and pneumonia, are leading causes of hospitalization and mortality in South Africa [1]. The health impact of respiratory diseases highlights the urgent need for reliable and rapid diagnostic tools capable of distinguishing between severe and mild respiratory illnesses as an aid to triage, as well as facilitating early diagnosis [2].

A key metric in the evaluation of pulmonary pathology is the peak expiratory flow rate (PEFR), which differs between healthy individuals and those with respiratory infections [3]. PEFR is commonly utilized to assess lung function in conditions such as pneumonia, bronchiectasis, and cavitary tuberculosis [3]. It represents the maximum expiratory velocity at which an individual can forcefully exhale air from the lungs [3].

Lungs affected by pulmonary conditions, including cavitary tuberculosis, pneumonia-related changes, and bronchiectasis, can significantly impact airflow dynamics and produce distinct acoustic patterns [4–6]. Vocalization encompasses any sound produced by the respiratory system and serves as an indicator of an individual's respiratory health [7]. Auscultation using a stethoscope remains a widely adopted, simple, and effective non-invasive method for detecting pulmonary abnormalities [8,9]. The sounds produced in the lungs are mainly characterized by impulsive noise and turbulent airflow. This noise arises from moving surfaces or surfaces subjected to uneven flow conditions [10,11]. Understanding the pathology and finding a diagnostic acoustic

* Corresponding author at: Clean Energy Research Group, Department of Mechanical and Aeronautical Engineering, University of Pretoria, Lynnwood Road, Hatfield, 0028, Pretoria, South Africa.
E-mail address: muaaz.bhamjee@up.ac.za (M. Bhamjee).

https://doi.org/10.1016/j.bspc.2026.110018
Received 16 July 2025; Received in revised form 8 February 2026; Accepted 1 March 2026
Available online 9 March 2026

change would aid in developing non-invasive diagnostic techniques and thereby improve patient outcomes.

Computational fluid dynamics (CFD) is an effective method for modelling airflow patterns and related acoustic phenomena within the respiratory system [12]. By integrating CFD with aero-acoustic modelling, researchers can analyse the impact of pathological conditions on flow-induced sound generation and propagation [12].

Faizel et al. [7] conducted a comprehensive review of CFD research aimed at investigating airflow behaviour within the human upper airway [7]. The development of high-performance computing has significantly enhanced the capacity to analyse complex patient-specific geometries under a range of physiological and surgical conditions [7]. This progress has facilitated improved diagnostics and preoperative planning [7]. Despite these advances, notable challenges and research gaps persist, particularly in the simulation of human airway mechanics and pulmonary dynamics.

A predominant focus of existing literature is on airflow modelling within the upper airway, with fewer studies addressing airflow dynamics beyond the primary bronchi, including deeper lung regions [7]. Additionally, understanding the implications of fluid–structure interactions remains limited, particularly given the anatomical variability across individuals and the influence of body posture on airway geometry and lung volumes [13,14]. Furthermore, airway morphology is dynamic throughout the respiratory cycle, leading to variations in flow resistance and particle deposition. These dynamic effects are often neglected in static airway models, potentially compromising the physiological accuracy of simulation outcomes [13].

This study aims to contribute to the ongoing efforts to enhance diagnostic options for lung pathologies by focusing on two key areas: gaining a deeper understanding of the fluid dynamics associated with various lung conditions and evaluating the potential of CFD to generate synthetic datasets for training artificial intelligence (AI) models designed for telemedicine-based diagnosis or triage. The study will analyse the aero-acoustic behaviours and vocalizations linked to lung-generated acoustics for selected pulmonary pathologies, namely pneumonia, bronchiectasis, and cavitary tuberculosis using CFD. This includes the development of models that accurately simulate realistic conditions for both healthy lungs and those affected by the aforementioned pathologies. To assess the effectiveness of CFD in accurately capturing the acoustic profiles of vocalizations related to different lung pathologies, the model predictions are validated using data from 22 vocal recordings (8 bronchiectasis recordings, 7 pneumonia recordings, 2 cavitary tuberculosis recordings, and 5 recordings from individuals approximately 24 months post recovery) of infected patients with distinct clinical diagnoses.[1]

2. Methodology

2.1. Modelling geometry and mesh

The lung geometry utilized in this study was obtained from North Carolina State University, representing a patient-specific model derived from earlier research conducted by Su et al. [15]. The model, illustrated in Fig. 1 [16], comprises four anatomical sections: the bronchus, trachea, larynx, and oropharynx. To ensure numerical stability at the boundary conditions, a tube extension was incorporated into the geometry, facilitating accurate fluid flow modelling at the oral cavity inlet and outlet. The inclusion of a tube extension at the inlet allows the airflow to stabilize and fully develop before entering complex airway geometries [15]. This inclusion results in simulations that more accurately represent physiological conditions and thereby improving the reliability of predictions related to downstream flow behaviour within the respiratory tract [15].

[1] Data source: Perinatal HIV Research Unit - University of the Witwatersrand. Ethics approval obtained from the University of Johannesburg (NHREC Registration: REC 241112–035).

This patient-specific model provides a detailed representation of individual anatomical features. This study, however, concentrates on the upper airway generations, where high-velocity airflow is the primary source of acoustic noise [7]. By concentrating on these regions, the model effectively captures key dynamics relevant to vocalization. Although derived from a single patient, the airflow characteristics in these upper airway regions are expected to be broadly applicable, as they are primarily influenced by geometric factors, airflow velocity, and local pressure variations that remain consistent among healthy individuals [7]. The lung model features bronchial branches up to the third generation and comprises 10 respiratory bronchioles.

The decision to use a third-generation bifurcation was done after reviewing other similar studies and based on the decision on the primary acoustic features and pulmonary disease patterns which are mainly expressed within the three generations. Extending the model further may introduce diminishing returns in terms of meaningful data, as the influence of more distant generations on the pulmonary acoustics become less significant. By focusing on the three generations, the model captures the key acoustic patterns that are most relevant to diagnosing and understanding pulmonary diseases, providing a balance between precision and computational feasibility [17,18]. Research in respiratory acoustics indicates that the airflow turbulence, breath sound characteristics, and pathological alternations such as wheezing and crackles are most prominently generated and modulated within the first three airway generations [17,18]. Beyond this point, sound transmission is increasingly attenuated, and additional generations contribute progressively less to meaningful diagnostic differentiation [17,18].

A tetrahedral mesh was employed, with an element size of 3 mm, resulting in a total of 10.1 million cells. A constant mesh size was used throughout. A mesh independence study was conducted to assess the appropriateness of the selected mesh resolution and to ensure result convergence. The study utilized the Grid Convergence Index (GCI) method, comparing mesh sizes of 3 mm, 6 mm, and 12 mm. Additionally, a time step sensitivity analysis was performed using the GCI method.

2.1.1. Mesh sensitivity study

The mesh independence study follows the GCI method by Roache [19], using three successively refined grids with a refinement ratio, r = 2, starting from a baseline mesh with a 3 mm cell size. As this analysis mirrors that of a previous study by the authors [16], only a brief summary is provided here. Surface acoustic power was used as the performance metric and evaluated consistently across all mesh resolutions. As shown in Table 1 [16], the asymptotic convergence ratios at positions 1 (100 mm), 2 (115 mm), and 3 (130 mm) approach unity, confirming mesh independence. A 3 mm mesh size was thus chosen for all simulations [16].

2.2. Governing equations

The core equations that describe fluid flow consist of the continuity equation, which ensures mass conservation, and the momentum conservation equations; together, these are referred to as the Navier–Stokes equations. This study incorporates turbulence effects using the Unsteady Reynolds-Averaged Navier–Stokes (URANS) equations, specifically employing the Realizable $k-\epsilon$ model, as well as the Large Eddy Simulation (LES) approach. To capture acoustic phenomena, turbulence models are integrated with appropriate aero-acoustic formulations: LES is coupled with the Ffowcs Williams and Hawkings (FW-H) model, while the Realizable $k-\epsilon$ model is paired with the Broadband Noise Source Model.

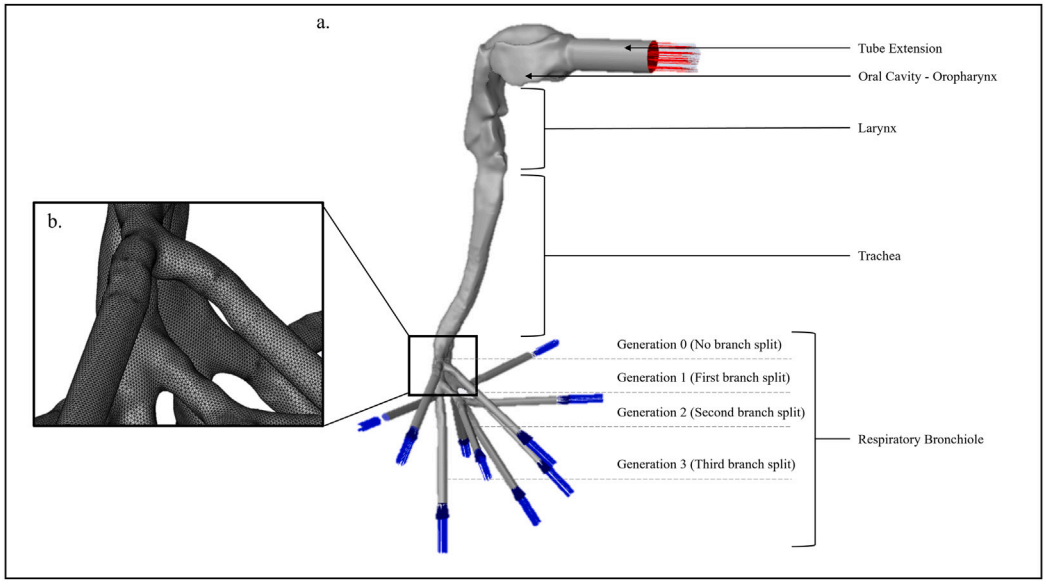

Fig. 1. Representative Geometry: (a) Lung structure showing labelled regions; and (b) Mesh representation of the lobar bronchus [16].

Table 1
Grid Convergence Index evaluation for surface acoustic power – Mesh independence study [16].

Position	f_1	f_2	f_3	GCI_{12}	GCI_{23}	Asymptotic range
(1) 100 mm	$6.5(10)^{-28}$	$6.4(10)^{-28}$	$5.8(10)^{-28}$	$3.84(10)^{-3}$	$2.34(10)^{-2}$	1.016
(2) 115 mm	$6.6(10)^{-28}$	$6.38(10)^{-28}$	$5.6(10)^{-28}$	$1.64(10)^{-2}$	$6(10)^{-2}$	1.034
(3) 130 mm	$6.4(10)^{-28}$	$6.3(10)^{-28}$	$5.7(10)^{-28}$	$3.91(10)^{-3}$	$2.38(10)^{-2}$	1.016

2.2.1. Governing equations - Realizable $k-\epsilon$ with the Broadband Noise Source Model

The Realizable $k-\epsilon$ turbulence model is the initial method employed in this study. A recognized limitation of this model is its reliance on wall distance, making it less effective for simulating free shear flows [20]. An underlying assumption in this apporach is that turbulence within the respiratory system is isotropic. This assumption is made to assess the applicability of aero-acoustics in diagnosing lung pathologies [21].

In the trachea and bronchi, airflow velocity is relatively low, allowing the flow to be considered incompressible [21]. The justification for this assumption is based on the flow conditions examined, as incompressibility is generally valid for flows with Mach numbers below 0.3, where density variations are negligible and do not significantly influence flow characteristics [21]. The assumption of isotropic turbulence serves as a simplification aimed at assessing the potential of aeroacoustics in identifying lung diseases.

The continuity equation due to the incompressibility of the flow simplifies to:

$$\frac{\partial u_i}{\partial x_i} = 0 \tag{1}$$

The momentum equation with Realizable $(k-\epsilon)$ model is,

$$\rho\frac{\partial u_i}{\partial t} + \rho\frac{\partial u_i u_j}{\partial x_j} = -\frac{\partial p}{\partial x_i} + \frac{\partial}{\partial x_j}\left[\mu\left(\frac{\partial u_i}{\partial x_j} + \frac{\partial u_j}{\partial x_j} - \frac{2}{3}\delta_{ij}\frac{\partial u_k}{x_k}\right)\right] - \rho\bar{g} - \rho\frac{\partial(\overline{u_i' u_j'})}{\partial x_j} \tag{2}$$

where the gravitational acceleration vector is $\bar{g} = (0, -9.81, 0)\ \mathrm{m/s^2}$. The transport equations for k and ϵ in the Realizable $k-\epsilon$ model are outlined below [14],

The instantaneous velocities (u_i) are composed of the mean $(\bar{u}_i)$ and fluctuating components (u_i') [22]:

$$u_i = \bar{u}_i + u_i' \tag{3}$$

Similarly, the instantaneous pressure (p) is given by:

$$p = \bar{p} + p' \tag{4}$$

$$\rho\frac{\partial}{\partial t}(k) + \rho\frac{\partial(k u_j)}{\partial x_j} = -\frac{\partial p}{\partial x_i} + \frac{\partial}{\partial x_j}\left[(\mu + \mu_t)\frac{\partial k}{\partial x_j}\right] + P_k - \rho\epsilon \tag{5}$$

where the turbulent viscosity, μ_t, for the Realizable $k-\epsilon$ model,

$$\mu_t = \rho C_\mu \frac{k^2}{\epsilon} \tag{6}$$

The production term of kinetic energy is denoted as P_k, and $\sigma_k = 1.0$ represents the turbulent Prandtl number for k. For the realizable $k-\epsilon$ model C_μ is not a constant. Instead it is computed from turbulence quantities such as the mean strain and rotation rates, the systems angular velocity as well as k and ϵ [22]. The dissipation rate (ϵ) equation is given by [14]:

$$\rho\frac{\partial \epsilon}{\partial t} + \rho\frac{\partial \epsilon u_j}{\partial x_j} = \frac{\partial}{\partial x_j}\left[\left(\mu + \frac{\mu_t}{\sigma_\epsilon}\right)\frac{\partial \epsilon}{\partial x_j}\right] + \rho C_1 S\epsilon - \rho C_2 \frac{\epsilon^2}{k + \sqrt{\nu\epsilon}} \tag{7}$$

where, C_1, $C_2 = 1.9$, and $\sigma_\epsilon = 1.2$ are model constants, and P_k represents the production term for turbulence kinetic energy. The constant C_1 is calculated using the following relationship [22]:

$$C_1 = max\left[0.43, \frac{\eta}{\eta + 5}\right], \eta = S\frac{k}{\epsilon}$$

The Boussinesq hypothesis relates Reynolds stresses to mean velocity gradients [14],

$$-\rho\overline{u_i' u_j'} = -2\mu_t\delta_{ij} = -\rho C_\mu \frac{k^2}{\epsilon}\left(\frac{\partial u_i}{\partial x_j} + \frac{\partial u_j}{\partial x_i}\right) \tag{8}$$

Proudman [23], leveraged Lighthill's [24] acoustic analogy to calculate the acoustic power produced by isotropic turbulence in the absence of mean flow [14]. Lilley [25] redeveloped this formula,incorporating the effect of the retarded time difference. These methods provide the acoustic power generated per unit volume of isotropic turbulence,

expressed in watts per cubic meter, W/m^3, as shown below [14]:

$$P_A = \alpha \rho_0 \left(\frac{u^3}{l}\right) \frac{u^5}{c_0^5} \tag{9}$$

where u and l represent the turbulence velocity and length scales [14]. This can be re-written in the form [22]:

$$P_A = \alpha_\epsilon \rho_0 \epsilon M_t^5 \tag{10}$$

where,

$$M_t = \frac{\sqrt{2k}}{c_0} \tag{11}$$

where $a_\epsilon = 0.1$, $\rho_0 = 1.225$ kg/m^3 and $c_0 = 340$ m/s. The turbulent kinetic energy (k) and the dissipation rate (ϵ) are calculated from the turbulent fields, which are calculated using Eqs. (5) and (7), respectively.

2.2.2. Governing equations - Large Eddy simulation and Ffowcs Williams and Hawkings model

LES is the second turbulence model used in this study. Unlike URANS, which resolves only the mean flow and an isotropic turbulence closure, LES explicitly captures large, energy-containing eddies while modelling smaller-scale turbulence using a subgrid-scale model [26]. Unlike the Realizable $k-\epsilon$ model, which assumes isotropic turbulence, LES accounts for turbulence anisotropy, making it more suitable for complex, transitional, or low-to-moderate Reynolds number flows [21,27]. The assumption of incompressibility is justified by the low Mach number, where density variations are negligible. Given the airflow velocities in the trachea and bronchi, this assumption simplifies the model without significantly affecting accuracy.

The continuity equation for incompressible flow:

$$\frac{\partial \bar{u}_i}{\partial x_i} = 0 \tag{12}$$

The momentum equations in LES are based on the Favre' filtered Navier–Stokes equations [21]:

$$\rho \frac{\partial \bar{u}_i}{\partial t} + \rho \bar{u}_j \frac{\partial \bar{u}_i}{\partial x_j} = \frac{\partial \bar{p}}{\partial x_i} + \frac{\partial}{\partial x_j}\left((\nu + \nu_t)\left(\frac{\partial \bar{u}_i}{\partial x_j} + \frac{\partial \bar{u}_j}{\partial x_i}\right)\right) - \rho \bar{g} \tag{13}$$

where $\bar{u}_i$ is the filtered velocity, $\bar{p}$ is the filtered pressure, ν is the molecular viscosity and ν_t is the eddy viscosity obtained from the subgrid-scale model. The chosen subgrid-scale model is the Wall-Adapting Local Eddy-Viscosity (WALE) model, which is specifically developed to accurately represent the asymptotic behaviour of turbulence in flows near walls. In incompressible flows, Reynolds stress asymptotics near the wall are governed by the constraint that the volume of fluid entering a given region must equal the volume exiting, ensuring mass conservation [28]. In the LES Ffowcs Williams and Hawkings model using ANSYS Fluent 2021R2® [29], the WALE subgrid-scale model is selected. Unlike the Smagorinsky model, which is more reliable for flows away from solid boundaries, the WALE model provides improved accuracy in predicting near-wall turbulence, making it more suitable for this study [21,30].

The eddy viscosity in WALE is defined as [21,30],

$$\nu_t = (C_w \Delta)^2 \frac{(S_{ij}^d S_{ij}^d)^{3/2}}{(S_{ij} S_{ij})^{5/2} + (S_{ij}^d S_{ij}^d)^{5/4}} \tag{14}$$

where C_w is the model constant (approximately 0.325), Δ is the filter width, S_{ij} is the strain-rate tensor, S_{ij}^d is the traceless symmetric component of the squared velocity gradient tensor. The WALE model specifically modifies the effective viscosity through the addition of the turbulent viscosity ν_t in the viscous stress term.

The Ffowcs Williams and Hawkings model expands on Lighthill's acoustic analogy, enabling the prediction of far-field noise produced by turbulent flows and moving surfaces [22]. It is particularly suited for compressible flows but can also be applied to incompressible flows in the low Mach number limit, such as respiratory airflow [22].

The Ffowcs Williams and Hawkings equation for the radiated acoustic pressure p' is given as [22]:

$$\frac{\partial^2 p'}{\partial t^2} - c_0^2 \frac{\partial^2 p'}{\partial x_i \partial x_i} = \frac{\partial}{\partial t}\left[Q(x_i,t)\right] + \frac{\partial}{\partial x_i}\left[F_i(x_i,t)\right] + T_{ij}(x_i,t) \tag{15}$$

where Q represents monopole (mass flux) sources, F_i dipole (force) sources, and T_{ij} quadrupole (turbulence stress) sources. For low Mach number flows, quadrupole contributions become negligible, simplifying the Ffowcs Williams and Hawkings model to surface integrals [22]. The generalized Ffowcs Williams and Hawkings equation in integral form over a permeable surface S enclosing a volume V is expressed as [22]:

$$p'(\mathbf{x},t) = \frac{1}{4\pi}\int_S \left[\frac{L_r}{r(1-M_r)^2}\right]_{\text{ret}} dS + \frac{1}{4\pi}\int_S \left[\frac{M_n \dot{L}_r}{r(1-M_r)^3}\right]_{\text{ret}} dS \tag{16}$$

where $L_r = \rho \bar{u}_i n_i$ is the loading term from surface pressure and normal velocity, $M_r = \bar{u}_i r_i / c_0$ is the local Mach number in the observer direction, $M_n = \bar{u}_i n_i / c_0$ is the normal Mach number, $\dot{L}_r$ is the time derivative of L_r. All terms are evaluated at the retarded time $t_r = t - r/c_0$.

The acoustic source terms in the Ffowcs Williams and Hawkings model are derived from the LES-resolved unsteady flow field [22]. In ANSYS Fluent [29], these inputs are directly extracted from surface pressure and velocity data. Since LES accurately resolves the large-scale turbulent structures responsible for sound generation, it enhances the prediction of unsteady surface fluctuations and improves the reliability of Ffowcs Williams and Hawkings acoustic results [22].

2.3. Boundary conditions and solver setup

2.3.1. Boundary conditions

The boundary conditions applied in this study are summarized in Table 2 [16]. The atmospheric pressure is set to the value of 101.325 kPa.

Volumetric flow rates are based on expected physiological conditions for the four cases analysed: healthy lungs (5 L/s), lungs with pneumonic changes, cavitary tuberculosis-infected lungs, and bronchiectatic lungs (all at 2.7 L/s) [10,11,31,32]. The inlet "cough" boundary condition was modelled to achieve the PEFR for each pathology. Consequently, a constant volumne flow rate was applied to the match the PEFR (pathology dependent). Thus, no time-dependent driving waveform was applied. Although the overall volumetric flow rate was maintained at 2.7 L/s across all infected lung models for consistency, pathology-specific variations were incorporated to reflect characteristic airflow alterations as seen in Fig. 2.

In the model representing pneumonia, reduced flow rates were applied in the bronchioles to simulate the impaired ventilation due to inflammatory changes [6]. For cavitary tuberculosis, localized disruption of airflow was modelled by introducing a cavity into one of the bronchioles, reflecting tissue destruction associated with the disease. In the case of bronchiectasis, which is characterized by bronchial dilation and chronic obstruction, a significantly reduced flow rate of 1.6 L/s was applied to a bronchiole to simulate the impaired airflow observed in severe cases [6].

The study focuses on the exhalation phase, modelling the bronchioles as the inlet and the mouth (tube extension) as the outlet. The CFD models incorporate standard assumptions, namely: (a) that a no-slip boundary condition exists at the adventitia (referred to as walls in CFD terminology), (b) the air is an incompressible fluid with a constant density of 1.225 kg/m^3 and (c) the air is considered a Newtonian fluid with constant viscosity, 1.7894×10^{-5} kg/m s, and steady static pressure [33]. These assumptions align with established methodologies in previous research [34–36]. The no-slip boundary condition, applied

Table 2
Boundary conditions applied in the model for different lung conditions [16].

Boundary	Type	Condition/Flow rate	Pressure (kPa)	Acoustic power (W)	Notes
Oral cavity	Pressure outlet	Atmospheric pressure	101.325	1×10^{-12}	Healthy/Diseased
Respiratory bronchiole (Inlet)	Velocity inlet	5.0 L/s (Healthy)	101.325	1×10^{-12}	Case dependent
Respiratory bronchiole (Inlet)	Velocity inlet	2.7 L/s (Pneumonia, Cavitary Tuberculosis, Bronchiectasis)	101.325	1×10^{-12}	Case dependent
Outlet	Outflow	N/A	101.325	1×10^{-12}	Applies to all cases
Wall (Oropharynx, Larynx, Trachea, Lobar Bronchus)	Wall boundary	No slip	N/A	N/A	Geometric walls

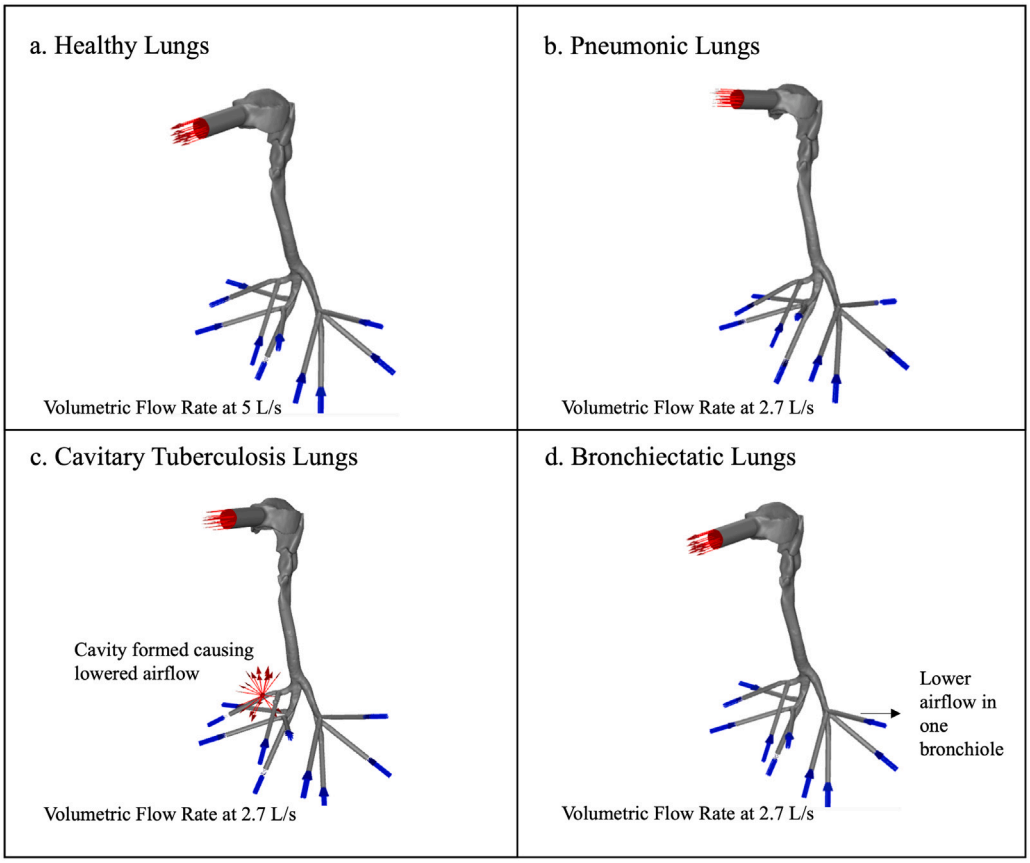

Fig. 2. Volumetric flow rate: (a) Healthy lungs; (b) Pneumonic lungs; (c) Cavitary tuberculosis lungs; and (d) Bronchiectactic lungs.

to the bronchioles, trachea, larynx, oral cavity, and tube extension, is expressed as:

$$u_w = 0 \tag{17}$$

Polyurethane, having a density of 949.79 kg/m^3, is used as a surrogate for the adventitia due to its similar density [3]. Although the adventitia walls are naturally flexible, they are modelled as rigid, and hydrostatic pressure is considered at the lung base. The research investigates aero-acoustic differences between healthy and diseased lungs, with future work suggested to incorporate flexible walls and fluid–structure interaction (FSI).

2.3.2. Solver setup

A hybrid initialization is implemented instead of standard initialization. Hybrid initialization is more accurate than standard initialization as it solves simplified equations to generate realistic initial flow fields that better reflect boundary conditions and domain geometry, leading to faster and more stable convergence, and reduced numerical errors [22]. This results in more precise estimates of flow variables from the outset [22]. This approach is beneficial when using segregated solvers like the Semi-Implicit Method for Pressure-Linked Equations (SIMPLE), as it provides a better starting point for the sequential solution process and helps stabilize the solution of turbulence transport equations, especially when first-order schemes are used for the turbulent kinetic energy (k) and dissipation rate (ϵ). Table 3 summarizes the solver settings used in the study. The combination of the SIMPLE algorithm with second-order pressure correction and first-order turbulence discretization reflects a deliberate balance between solution accuracy, computational efficiency, and numerical stability. These choices were made in accordance with the flow characteristics and the computational limitations of the study.

2.4. Time step sensitivity study

A time step independence study was conducted in a previous study by the authors [16], maintaining a constant mesh cell size of 3 mm while varying the time steps to 1 s, 0.1 s, 0.01 s, and 0.001 s [16]. Convergence was attained for all time steps except at 1 s. The Grid Convergence Index method was used, with surface acoustic power on the larynx serving as the performance metric. Results, presented in

Table 3
Solver settings - Realizable $k-\epsilon$ with Broadband Noise Source and LES with Ffowcs Williams and Hawkings [16].

Solver settings	Value
Number of time steps	100
Time step size (s)	0.1
Max iterations/Time step	20
Pressure velocity coupling—Type	Simple
Discretization scheme—Pressure	2nd order
Discretization scheme—Momentum	2nd order upwind
Discretization scheme—Turbulent kinetic energy	1st order upwind
Discretization scheme—Turbulent dissipation rate	1st order upwind

Table 4 summarizes the time step size study and illustrates asymptotic convergence and compliance with the Courant–Friedrichs–Lewy (CFL) condition, which requires a Courant number less than or equal to 1. A minor change of 1.69% in surface acoustic power was observed between the 0.1 s and 0.01 s time steps, and no significant change occurred between 0.01 s and 0.001 s. Based on these findings, a mesh size of 3 mm and a time step of 0.1 s were selected, satisfying the CFL condition with a Courant number of 5.3×10^{-2}.

3. Experimental data collection processing

To validate the CFD simulations, vocal recordings, particularly cough sounds, are analysed using the Fast Fourier Transform (FFT) via the Audacity software [37]. The vocal recordings were obtained from the Pertinatal HIV Research Unit (PHRU) as part of a study on community-acquired pneumonia (CAP) incidence, recurrence, and outcomes before and during the COVID-19 pandemic [38]. The dataset comprises of 22 recordings from patients hospitalized with severe pulmonary infections, including cavitary tuberculosis, pneumonia, and bronchiectasis, along with five additional recordings from patients approximately 24 months post-diagnosis to assess recovery-related acoustic changes [38]. The recordings are provided in waveform (.wav), MPEG-4 Audio (.m4a), and advanced audio coding (.aac) formats.

This section outlines the methodology for analysing vocal recordings obtained from the PHRU to identify pulmonary disease. The focus was on cough recordings, as coughing is a prevalent symptom in respiratory infections, observed in all 22 patient samples. Coughing occurs during exhalation, when the lungs contract and expel fluid, making it a critical marker for analysis. Speech data was excluded due to inconsistencies in patient responses.

The analysis of the sound recordings do not serve as a full clinical validation but rather as a feasibility investigation to determine whether the CFD-derived aero-acoustics can qualitatively reproduce cough-related spectral trends across key pulmonary pathologies, namely, pneumonia, cavitary tuberculosis, and bronchiectasis. The dataset composition is: 8 bronchiectasis recordings, 7 pneumonia recordings, 2 cavitary tuberculosis recordings, and 5 recordings from individuals approximately 24-months post-recovery.

Each recording contained at least one cough segment, although the clinical team did not annotate cough count per subject, as samples were collected opportunistically during routine clinical workflow. Healthy (recovered lung) recordings were not obtained under acoustically identical conditions, and we now emphasize that these may still reflect residual postinfection physiology. Because the PHRU clinical study did not standardize microphone type, distance, angle, room acoustics, or calibration procedures, reliance is placed on normalized spectral data rather than absolute SPL, supported by Savitzky–Golay smoothing, confidence bounds, and reduced χ^2 analyses that compare spectral shape rather than magnitude. Although broad cross-validation is not feasible with a dataset of this size, the study already incorporates several quantitative assessments including reduced χ^2 values for each pathology, Root Mean Squared Error, correlation coefficients, skewness, kurtosis, and fractional uncertainty bounds which have been made more prominent.

The data collection and processing methodology is as follows:

1. Data Acquisition - Obtain 22 vocal recordings from PHRU.
2. Format Conversion - Convert audio files from AAC to WAV to retain uncompressed audio data.
3. Software Processing - Import recordings into Audacity for spectral analysis.
4. Cough Identification - Manually detect cough segments.
5. Spectral Analysis - Utilize Audacity's FFT algorithm to generate frequency (Hz) vs. amplitude (dB) spectra.
6. Data Extraction - Download and analyse spectral plots.
7. Graphical Representation - Plot spectral data.
8. Repetition - Repeat steps 3–7 for all cough segments.
9. Apply a smoothing algorithm/filter on the spectral data using the Savitzky-Golay filter.

3.1. Plot spectrum using fast fourier transform in Audacity

The frequency spectrum graph is generated by applying a FFT to the selected audio signal, which is treated as a time series of sampled sound pressure values [37]. The FFT converts this time-domain data into the frequency domain, producing amplitude (in decibels, dB) across frequency (in hertz, Hz). Each frequency band indicates the strength or intensity of that frequency in the original signal, and these values are interpolated to form the graph. A detailed mathematical explanation of the FFT is provided below.

Step 1. Audio Signal Representation:

An audio signal in the time domain is represented as a discrete sequence of samples [37]:

$$x[n], \quad n = 0, 1, 2, \ldots, N-1 \tag{18}$$

where $x[n]$ is the amplitude at the nth sample, and N is the total number of samples. The sampling rate F_s defines the maximum recoverable frequency during the FFT process.

Step 2. Windowing:

To reduce spectral leakage, a Hanning window is applied [37]:

$$w[n] = 0.5\left(1 - \cos\left(\frac{2\pi n}{N-1}\right)\right), \quad n = 0, 1, 2, \ldots, N-1 \tag{19}$$

The windowed signal is:

$$x_w[n] = x[n] \cdot w[n] \tag{20}$$

Step 3. Fast Fourier Transform (FFT)[2]:

The FFT converts the time-domain signal to the frequency domain [37]:

$$X[k] = \sum_{n=0}^{N-1} x_w[n] \cdot e^{-j\frac{2\pi kn}{N}}, \quad k = 0, 1, 2, \ldots, N-1 \tag{21}$$

Step 4. Magnitude Calculation:

For $X[k] = a + jb$, the magnitude is computed as [37]:

$$|X[k]| = \sqrt{a^2 + b^2} \tag{22}$$

Step 5. Logarithmic Scaling:

The magnitude is converted to the normalized Sound Pressure Level (SPL) in dB via [37]:

$$SPL(dB) = 20\log_{10}|X[k]| \tag{23}$$

Step 6. Frequency Binning:

Due to symmetry in the FFT output, only the first $N/2$ bins are used [37]:

$$f[k] = \frac{kF_s}{N}, \quad k = 0, 1, 2, \ldots, \frac{N}{2} - 1 \tag{24}$$

[2] The indices i, j, k when used as summation indices do not represent the spatial dimensions i, j, k as used in the governing equations.

Table 4
Time step size independence study summary [16].

Time step (s)	Δx (mm)	Velocity magnitude (m/s)	CFL	Surface acoustic power (W/m^2)	Convergence achieved
1	3	$1.6(10)^{-3}$	$5.3(10)^{-1}$	$2.00(10)^{-27}$	No
0.1	3	$1.6(10)^{-3}$	$5.3(10)^{-2}$	$2.36(10)^{-27}$	Yes
0.01	3	$1.6(10)^{-3}$	$5.3(10)^{-3}$	$2.40(10)^{-27}$	Yes
0.001	3	$1.6(10)^{-3}$	$5(10)^{-4}$	$2.40(10)^{-27}$	Yes

7. Spectrum Plotting:

The spectrum is plotted with frequency $f[k]$ on the x-axis and Magnitude (dB) on the y-axis.

The FFT was implemented using the following parameters; a FFT length of $N = 1024$, an overlap of 50%, a frequency resolution of 2 Hz and a Hanning (Hann) Window.

3.2. Data smoothing/filtering

The Savitzky-Golay filter was selected for smoothing/filtering of the raw spectral data signals. It was selected for its ability to preserve local features such as peaks and troughs, which are often distorted by simpler methods like moving averages [39]. It operates by fitting a polynomial to a local subset of data via least squares and computing the smoothed value at the central point [39]. The chosen parameters strikes a balance between noise reduction and feature preservation, with the window size selected to avoid excessive smoothing or retention of noise.

For a window size of 11 points, the general polynomial fit used in the Savitzky-Golay filter is given by [39]:

$$\hat{y}(x) = a_0 + a_1 x + a_2 x^2 + \cdots + a_k x^k \tag{25}$$

where $\hat{y}(x)$ is the polynomial approximation, and x denotes the relative position of each data point inside the window.

The coefficients $a_0, a_1, \ldots, a_k$ are determined by minimizing the sum of squared differences between the actual and approximated values [39]:

$$\min \sum_{i=-5}^{5} \left(y_{j+i} - (a_0 + a_1 x + a_2 x^2 + \cdots + a_k x^k) \right)^2 \tag{26}$$

For a window size of 11, the smoothed value $\hat{y}_j$ at the central point y_j is computed using convolution coefficients C_i as follows [39]:

$$\hat{y}_j = \sum_{i=-5}^{5} C_i y_{j+i} \tag{27}$$

Here, y_{j+i} are the original data points within the window, and C_i are the precomputed convolution coefficients corresponding to the filter parameters. The standard deviation of the smoothed signal is estimated as [39]:

$$\sigma = \sigma_1 \sqrt{\sum c_j^2} \tag{28}$$

where c_j are the Savitzky-Golay filter coefficients, and σ_1 is the standard deviation of the data before smoothing is applied.

3.3. Experimental results

Fig. 3 presents the experimental results, comparing sound pressure levels (SPL) between healthy and infected lungs. The solid line shows SPL smoothed using a Savitzky-Golay filter (n = 11), while dashed lines indicate variability bounds.

Both healthy and infected lungs exhibit peak frequencies between 0.4–0.6 kHz. Healthy lungs reach a maximum SPL of 70 dB and maintain the highest average SPL across the 0–11 kHz range. A sharp decline in SPL at 11 kHz is observed in healthy lungs, likely due to high-frequency scattering and reduced transmission [40]. Literature reports peak frequencies near 1.6 kHz in healthy individuals [41].

However, the samples in this study that represent healthy lungs were from patients who have recovered from lung infections - possibly retaining long-term physiological changes even 24 months post-diagnosis. A gradual SPL decline is evident from 8 kHz onwards in both groups; in cavitary tuberculosis, low-frequency sounds at cavity regions and disrupted airflow may explain this trend [5]. Additionally, lungs with bronchiectasis and pneumonic changes show similar SPL-frequency profiles. This similarity may stem from patients with prior bronchiectasis developing pneumonia, as the condition predisposes individuals to infection due to fluid and pus accumulation in the air sacs [4].

4. Simulation results

The primary goal is to validate the model results for different lung pathologies by comparing them with the cough recordings shown in Fig. 3. This comparison is important because the amplitude of cough signals can vary significantly due to factors such as differences in recording equipment sensitivity, individual vocal effort, or scaling parameters used in the simulation [42]. To account for these variations and ensure a fair comparison, all signals are rescaled to a consistent reference level using a linear scaling approach. This method applies a frequency-independent scaling factor based on the average sound pressure level, in decibels, across the spectrum, chosen for its simplicity and ease of interpretation. To further aid in comparing the frequency-domain trends between the CFD results and the recorded cough data, a smoothing technique, specifically, a Savitzky-Golay filter with a window size of n = 11 is applied to both datasets to highlight overall trends and reduce noise.

4.1. Evaluation of simulation accuracy against experimental data

To evaluate the accuracy of the model relative to the recorded data, statistical hypothesis testing was employed using the χ^2 method. This approach was implemented to assess variations in distribution between the simulation results and the experimental data. The reduced χ^2 statistic, shown in Eq. (29), is a standard metric in statistical model fitting used to quantify the goodness of fit [39]. This metric facilitates comparison across models or datasets with differing degrees of freedom, thereby enabling standardized assessment of fit quality [39]. Additionally, the χ^2 statistic, Eq. (31), provides a measure of the total deviation between observed and expected values, commonly applied in hypothesis testing [39].

$$\chi^2_{\text{red}} = \frac{\chi^2}{\nu} = \frac{1}{\nu} \sum_{i=1}^{N} \left(\frac{O_i - E_i}{\sigma_i} \right)^2 \tag{29}$$

$$\sigma_i = \sqrt{\sigma^2_{\text{sim},i} + \sigma^2_{\text{data},i}} \tag{30}$$

$$\chi^2 = \sum_{i=1}^{N} \left(\frac{O_i - E_i}{\sigma_i} \right)^2 \tag{31}$$

where χ^2 is the χ^2 statistic, χ^2_{red} is the reduced χ^2 statistic, ν is the number of degrees of freedom, O_i represents the observed data values, E_i represents the expected (simulated) values and σ_i is the combined standard deviation of simulation and data uncertainties.

The null hypothesis assumes that the simulation accurately represents the situation and that the experimental data follows a normal distribution around the simulation. A 95% right-sided confidence limit $\alpha = 0.05$ is used to evaluate the null hypothesis. For lung pathologies, the χ^2 distribution with 332 degrees of freedom gives a critical value of approximately 375.2, corresponding to a reduced χ^2 value of about

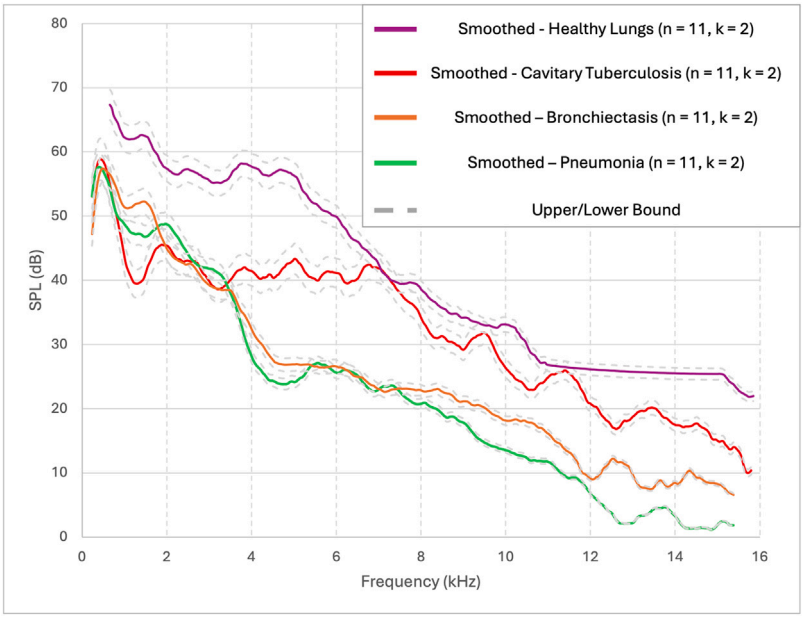

Fig. 3. Sound Pressure Level (SPL) vs. frequency (kHz) with smoothed data and confidence bounds – Healthy lungs and infected lungs.

Table 5
Reduced and observed χ^2 values for four lung conditions.

	Cavitary tuberculosis	Bronchiectasis	Pneumonia	Healthy lungs
Degree of freedom	332	332	332	258
Confidence limit	95%	95%	95%	95%
χ^2 critical value	375.2	375.2	375.2	300.33
χ^2	84.41	6.18	11.91	2.45
Reduced χ^2 (Critical)	1.130	1.130	1.130	1.165
LES with FW-H (Observed χ^2)	4.118	1.133	1.707	1.166
Realizable k-ϵ with Broadband Noise (Observed χ^2)	1.820	4.574	1.417	1.468

1.130. For healthy lungs, with 258 degrees of freedom, the critical value is approximately 300.33, resulting in a reduced χ^2 value of about 1.165. A χ^2 test is conducted at a significance level of $\alpha = 0.05$ to assess the goodness of fit between the model and the data. If the reduced χ^2 value is approximately 1, the model fits the data well. Values significantly greater than 1 indicate poor model fit or invalid assumptions, while values much smaller than 1 suggest model overfitting or overestimated uncertainties [43]. The decision to reject or accept the null hypothesis depends on whether the χ^2 value exceeds or is less than the critical value as calculated by Eq. (31) [43].

For both healthy lungs and diseased lung pathologies, the critical value corresponds to a 95% confidence limit $\alpha = 0.05$. The reduced χ^2 values were calculated using Eq. (29). The reduced χ^2 (χ^2_ν) statistic is commonly employed in statistical model fitting to evaluate the goodness of fit. A reduced χ^2 value close to 1 indicates that the observed data align well with the expected data under a specified statistical model. Table 5 summarizes the reduced χ^2 values for different pulmonary pathologies and healthy lungs using the two acoustic modelling approaches. While the additional statistical analyses provided in Table 6 shows additional quantitative assessment of model performance across respiratory conditions and the overall trends are consistent with the conclusions drawn from the reduced χ^2 analysis.

Table 7 includes the confidence limit and interprets the results to indicate whether the null hypothesis has been accepted or rejected.

In Fig. 4, and the data from Table 5, showing the healthy lungs, the LES with the Ffowcs Williams and Hawkings model yields a reduced χ^2 value of 1.166. The Realizable $k-\epsilon$ with the broadband noise source model produces a higher value of 1.468, and is less accurate than the LES model. Overall, the null hypothesis is rejected for both models.

Fig. 5 presents a frequency versus sound pressure level graph for a lung with cavitary tuberculosis, a condition characterized by hollow spaces in the lungs [5]. The figure compares simulated models with experimental data, revealing distinct patterns: a gradual slope at lower frequencies and a steep slope at higher frequencies. The experimental data shows sharper peaks and valleys at lower frequencies, while the LES with Ffowcs Williams and Hawkings model exhibits smoother transitions. During the explosive phase (0–2 kHz), both the LES with Ffowcs Williams and Hawkings and the Realizable $k-\epsilon$ with the Broadband Noise Source model display the highest sound pressure levels, which decrease during the intermediate phase (2–8 kHz) [44]. Beyond 8 kHz, the experimental data declines steadily, with the Realizable $k-\epsilon$ model showing a gradual decrease between 6–16 kHz, while the LES model declines sharply from 12–16 kHz. At 12 kHz, representing the tail-end of the intermediate phase, the patient cough recording reaches the lowest sound pressure level as muscle relaxation occurs [44]. As indicated in Table 5, the reduced χ^2 value for the LES with Ffowcs Williams and Hawkings model (4.118) and the Realizable $k-\epsilon$ model (1.820) both exceed 1, indicating poor model fit or underestimated uncertainties. Although neither model fits the data perfectly, the Realizable $k-\epsilon$ with the Broadband Noise Source model performs better, leading to the rejection of the null hypothesis.

Fig. 6 shows the frequency versus sound pressure level for lungs with pneumonic changes. Pneumonia inflames the air sacs, filling them with fluid and causing breathing difficulties [4]. Both the Realizable $k-\epsilon$ with the Broadband Noise Source model and the LES with the Ffowcs Williams and Hawkings model follow the general declining trend of the experimental data. The Realizable $k-\epsilon$ model aligns more closely with the experimental curve from 6 kHz onward, while the LES model matches better between 4 kHz and 8 kHz and beyond 8 kHz. The experimental data indicates a sound pressure level increase below 1 kHz during the explosive phase, followed by a decline from 1 kHz to

Table 6
Comparative statistical metrics for LES with FW-H and Realizable k-ϵ with Broadband Noise models across different respiratory conditions.

Metric	Cavitary tuberculosis		Pneumonia		Bronchiectasis		Healthy lungs	
	LES with FW-H	Realizable k-ϵ	LES with FW-H	Realizable k-ϵ with BNS	LES with FW-H	Realizable k-ϵ with BNS	LES with FW-H	Realizable k-ϵ with BNS
Reduced χ^2 (Observed χ^2)	4.118	1.820	1.707	1.417	1.133	4.574	1.166	1.468
Root Mean Square Error (dB)	0.269	0.166	0.088	0.084	0.087	0.217	0.054	0.067
Correlation coefficient SPL (dB)	0.847	0.861	0.961	0.986	0.966	0.889	0.986	0.979
Kurtosis	0.870	−0.737	−1.149	−1.070	−1.125	−1.736	−1.500	−1.207
Skewness	−1.458	0.781	0.641	0.478	0.658	−0.128	0.429	0.439

Table 7
χ^2 test results for lung condition models at 95% confidence level.

Parameter	Cavitary tuberculosis	Bronchiectasis	Pneumonia	Healthy lungs
Confidence limit (95%)	Accept	Accept	Accept	Accept
Reduced χ^2 value ($\chi_{critical}$)	1.13	1.13	1.13	1.165
LES with FW-H ($\chi_{observed}$)	4.118	1.133	1.707	1.166
LES with FW-H (Rejected/Accepted)	Rejected	Rejected	Rejected	Rejected
Realizable k-ϵ with Broadband Noise ($\chi_{observed}$)	1.82	4.574	1.417	1.468
Realizable k-ϵ with Broadband Noise (Rejected/Accepted)	Rejected	Rejected	Rejected	Rejected

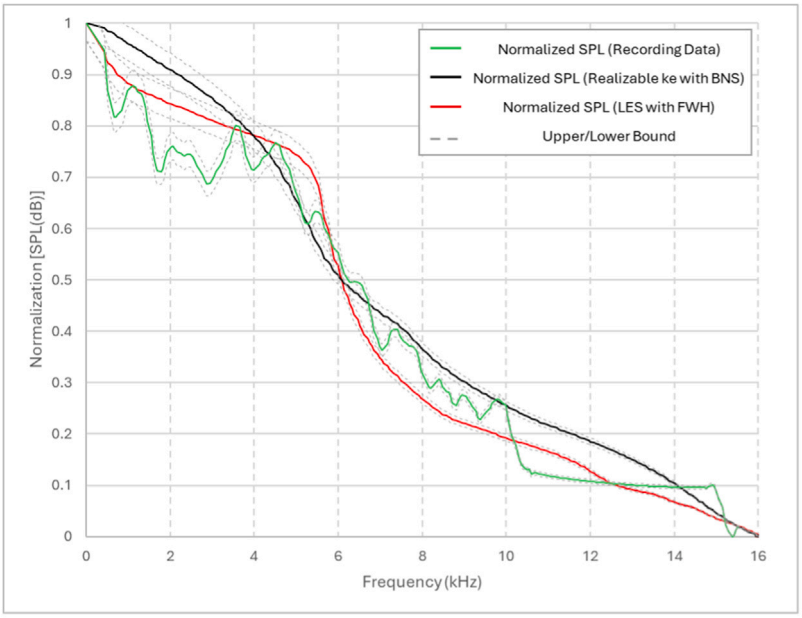

Fig. 4. Comparison of normalized Sound Pressure Level (SPL) vs. frequency for healthy lung data: Actual recording data, Realizable $k-\epsilon$ with Broadband Noise Source Model (BNS), and Large Eddy Simulation with Ffowcs Williams-Hawkings (LES with FW-H).

4 kHz, and a steep drop between 3 kHz and 5 kHz. After 6 kHz, both models align more closely with experimental results, showing a steady decline up to 11 kHz. As indicated in Table 5, the reduced χ^2 value for the LES model is 1.707, indicating a poor fit. The Realizable $k-\epsilon$ model has a lower value of 1.417, suggesting a better but still imperfect fit. Both models lead to rejecting the null hypothesis.

Fig. 7 shows the frequency versus sound pressure level for a bronchiectatic lung. Bronchiectasis slows airflow and, when severe, impairs breathing [6]. At lower frequencies, the LES with the Ffowcs Williams and Hawkings model aligns more closely with the experimental data than the Realizable $k-\epsilon$ with the Broadband Noise Source model. Both models follow the experimental trend of a steady decline above 8 kHz. During the explosive phase (0–2 kHz), both models show the highest sound pressure levels. Around 12 kHz, all three datasets exhibit a steep decline up to 16 kHz. As indicated in Table 5, the reduced χ^2 value for the LES model is 1.133. In contrast, the Realizable $k-\epsilon$ model has a value of 4.574, suggesting a poor fit. Thus, the null hypothesis is not rejected for the LES model but is rejected for the Realizable $k-\epsilon$ model.

Statistically the null-hypothesis is rejected in all cases. However, the results illustrate hypothesis-generating insights based on the qualitative agreement between the CFD-derived acoustics and the cough data. Based on the qualitative agreement between the CFD-derived acoustics and the cough analysis, it can be said that the LES with the Ffowcs Williams model has potential to reproduce the acoustics of the pathologies under study except the case of cavitary tuberculosis.

The comparative performance between the LES and the Realizable $k-\epsilon$ models can be attributed to the fundamental differences in how each model handles turbulence and flow-acoustic interactions. LES resolves the larger turbulent eddies directly while modelling only the smaller scales, which enables it to capture transient and spatial variations in airflow more accurately [45]. This makes LES particularly effective for simulating the complex, irregular flow structures present in bronchiectasis, where localized turbulence and distorted airway geometry lead to pronounced unsteady flow and acoustic fluctuations [45]. In contrast, the Realizable $k-\epsilon$ model, relies on time-averaged equations and turbulence models derived from the Boussinesq hypothesis [21,27,

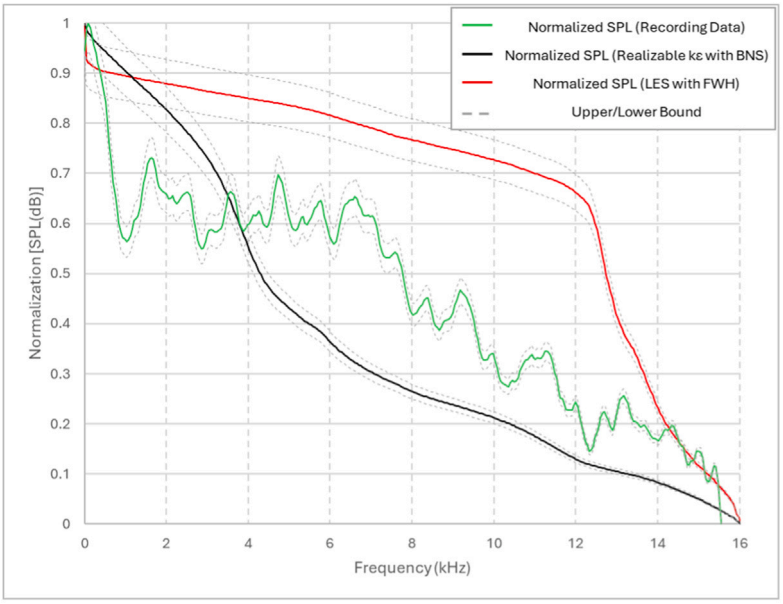

Fig. 5. Comparison of normalized Sound Pressure Level (SPL) vs. frequency for cavitary tuberculosis data: Actual recording data, Realizable $k-\epsilon$ with Broadband Noise Source Model (BNS), and Large Eddy Simulation with Ffowcs Williams and Hawkings (LES with FW-H).

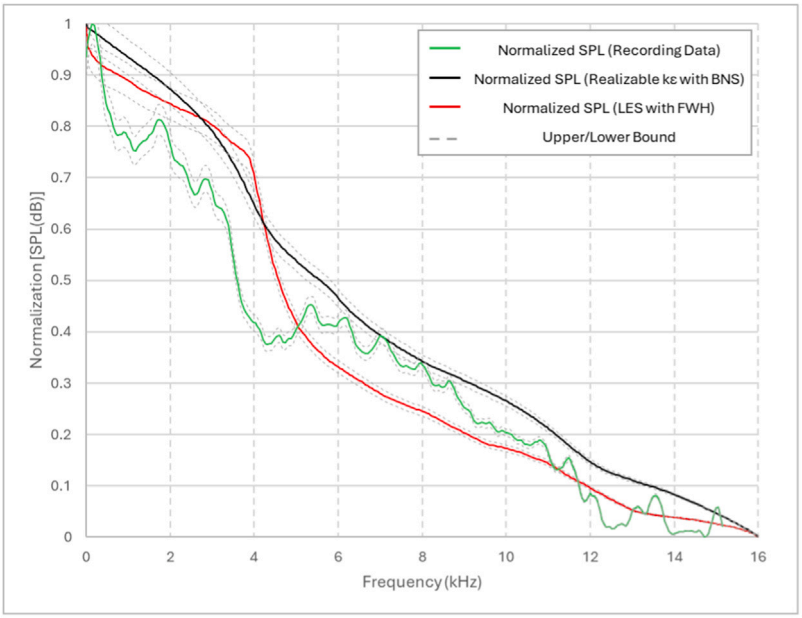

Fig. 6. Comparison of normalized Sound Pressure Level (SPL) vs. frequency for pneumonia data: Actual recording data, Realizable $k-\epsilon$ with Broadband Noise Source Model (BNS), and Large Eddy Simulation with Ffowcs Williams-Hawkings (LES with FW-H).

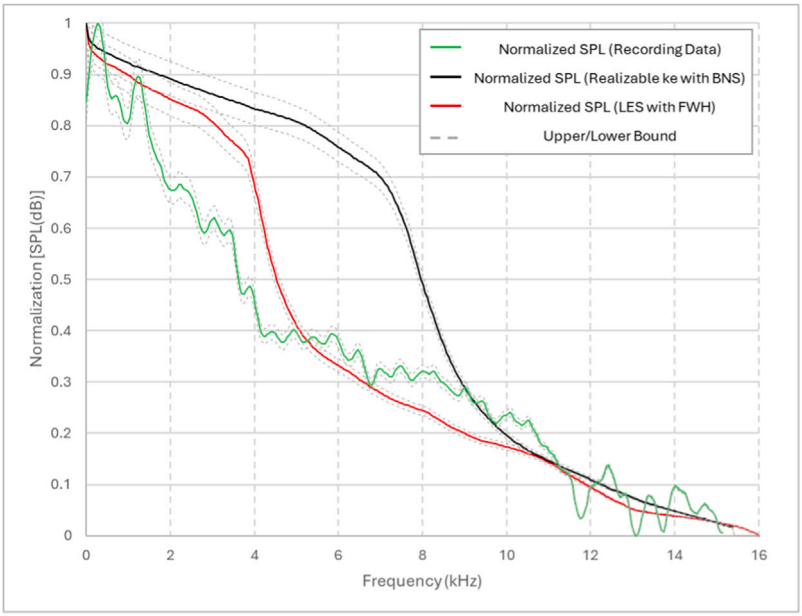

Fig. 7. Comparison of normalized Sound Pressure Level (SPL) vs. frequency for bronchiectasis data: Actual recording data, Realizable $k-\epsilon$ with Broadband Noise Source Model (BNS), and Large Eddy Simulation with Ffowcs Williams-Hawkings (LES with FW-H).

45]. While the Realizable $k-\epsilon$ model cannot resolve instantaneous flow fluctuations, it offers robust and computationally efficient predictions of mean flow characteristics [45]. This makes it more suitable for conditions such as pneumonia, where airflow is relatively less chaotic and the acoustic response is dominated by higher-frequency but less spatially complex noise sources.

The observed differences in model performance comes from their respective turbulence treatment strategies. LES excels in resolving detailed flow structures and low-frequency unsteady noise in complex, distorted airways, whereas the Realizable $k-\epsilon$ model performs better in predicting broadband noise behaviour at higher frequencies where mean flow properties dominate. The complementary strengths of both models thus provide a more complete understanding of pulmonary airflow acoustics across different disease states.

A key consideration in selecting a turbulence model is the trade-off between computational cost and model accuracy, particularly in applications such as real-time telemedicine diagnostics where rapid processing is essential. Direct Numerical Simulation (DNS), while offering the highest fidelity, is computationally prohibitive as its grid requirement scales with the Reynolds number to the power of $Re^{9/4}$ [46]. Large Eddy Simulation (LES) reduces this cost to a scaling of $Re^{9/5}$ by resolving large-scale eddies and modelling smaller turbulent structures, but it still demands a fine, high-quality boundary mesh and substantial computational resources [21,46]. The Detached Eddy Simulation (DES) method offers a practical compromise by combining the strengths of LES and RANS, thereby achieving lower computational expense while maintaining reasonable accuracy for unsteady flow features [46]. In contrast, RANS-based models such as the Realizable k–ϵ and k–ω formulations are significantly less demanding computationally, making them attractive for applications that require large-scale or real-time data generation [46].

In the study, the comparison of the computational performance between the LES and Realizable k–ϵ models revealed distinct differences in efficiency and practical applicability. The LES models exhibited longer case and data reading times and required higher peak virtual memory, indicating a greater overall computational demand. In contrast, the Realizable k–ϵ model initialized more quickly and maintained a lower total memory footprint, although it showed marginally higher memory usage per computational cell.

From a practical standpoint, these differences have meaningful implications for applied and data-driven research. The lower computational requirements of the Realizable k–ϵ model make it particularly suitable for large-scale or near-real-time applications, such as generating extensive synthetic datasets for telemedicine diagnostics. Conversely, the LES model, while more resource-intensive, remains valuable for high-fidelity investigations where detailed transient flow structures are of primary interest. Thus, model selection should be guided by the intended application, balancing the need for accuracy with computational efficiency.

5. Conclusion

This research paper validated CFD simulation models against experimental lung pathology data and provided insights into lung dynamics across various conditions. The analysis compared the LES with the Ffowcs Williams and Hawkings model and the Realizable $k-\epsilon$ model with the Broadband Noise Source against experimental recordings of healthy and diseased lungs. Results indicated that both models demonstrated qualitative agreement with experimental data for healthy lungs, pneumonia, and bronchiectasis, but failed to capture the complex aeroacoustics behaviour of cavitary tuberculosis accurately. Among the two models, the LES with the Ffowcs Williams and Hawkings model exhibited better qualitative performance across all pathologies except cavitary tuberculosis, where neither model was sufficient.

For healthy lungs, both models captured the decreasing sound pressure level with increasing frequency. In the case of pneumonia, the Realizable $k-\epsilon$ model aligned more closely with experimental data at higher frequencies. For bronchiectasis, the LES model showed a better match at lower frequencies, while both models followed the experimental trend at higher frequencies. However, for cavitary tuberculosis, significant deviations were observed, highlighting the need for model refinement. The use of CFD methods effectively illustrated airflow characteristics, including expiration pressure and velocity magnitude, which aligned with established literature. The lower computational demand of the Realizable k–ϵ model in comparison to LES, makes it particularly suitable for producing large synthetic datasets and for integration into near real-time diagnostic frameworks, where computational efficiency is critical to clinical feasibility. The insights provided by these simulations demonstrate the potential of CFD in differentiating lung pathologies based on acoustic signatures.

5.1. Research limitations and future work

Several limitations were identified in the study. First, the lung model only included three generations of bronchioles, whereas real airways exhibit 23 generations, possibly limiting anatomical generalizability. By focusing on the three generations, the model captures the key acoustic patterns that are most relevant to diagnosing and understanding pulmonary diseases, providing a balance between precision and computational feasibility. For future work, this can be further explored as high resolution and high sensitivity phase contrast tomographic images of healthy and diseased lungs are becoming available in the Human Organ Atlas project [47,48]. These could be used to generate additional depth in the biophysical bronchial models. Second, the models assumed uniform lung elasticity, oversimplifying the heterogeneous material properties of lung tissue. Incorporating advanced material models or using animal models with structural similarities to human lungs could enhance future simulations.

Third, the absence of patient-specific anatomical data, including detailed radiological images, restricted the model's ability to account for individual variability. Fourth, pulmonary diseases were grouped without distinguishing between stages, reducing the precision of disease representation. Fifth, the assumption of constant airflow velocity simplified the complex dynamics of the respiratory system, excluding factors such as lung volume changes and airway resistance. A final limitation for the research is not refining the modelling of pneumonia by incorporating a porous media approach. This would enable the simulation to account for the liquid accumulation in the alveolar regions, thereby improving the acoustic and flow predictions in pneumonia infected lungs.

It should be noted that inter-subject variability and disease-stage stratification were unavailable. Flow-rate conditions were selected based on established PEFR values, with pathology-specific airflow disruption incorporated; however, systematic sensitivity analyses for varying cough strength, airway geometry, and breathing patterns were beyond the scope of this study. Generalizability is constrained by the small dataset, heterogeneous acquisition conditions, lack of calibration, absence of patient-specific anatomical data, single-scenario flow-rates, and lack of disease-stage detail. Despite these limitations this study does provide a platform for future work on larger sample sizes.

Future research should integrate patient-specific geometries, improved material properties, a larger sample size and dynamic airflow patterns for more accurate simulations. Additionally, incorporating machine learning offers promising potential for enhancing disease classification by combining CFD-generated synthetic datasets with real-world clinical data. While the current results are mesh independent, future studies employing LES should address the stricter meshing requirements. This could include maintaining wall-resolved mesh conditions such as $y^+ \approx 1$, and ensuring that the streamwise (x^+) and spanwise (z^+) resolutions are similarly within order unity. This is necessary for accurately capturing the near-wall turbulent structures that significantly influence acoustic generation and propagation in pulmonary flows.

This study leverages well established methods, namely, standard URANS/LES turbulence models (the Realizable $k-\epsilon$ and LES-WALE models), classical FW-H and broadband noise source formulations, and a simplified three-generation bronchial tree, all of which have already been widely used for airway flow and sound simulations. The novelty of this study lies in the application of these trusted models; specifically, gaining hypothesis-generating insights of the aero-acoustics associated with various lung conditions and evaluating the potential of CFD to generate synthetic datasets for training artificial intelligence (AI) models designed for telemedicine-based diagnosis or triage. Furthermore, the study provides an in-depth statistical analysis with deep scientific interpretation of the CFD results, benchmarked against the actual recordings of vocalizations collected from people with defined lung pathologies. This data provides robust validation of the CFD results and provides validation (albeit on a small sample size) of the CFD models.

CRediT authorship contribution statement

Khanyisani Mhlangano Makhanya: Writing – review & editing, Writing – original draft, Visualization, Validation, Software, Project administration, Methodology, Investigation, Formal analysis, Data curation, Conceptualization. **Muaaz Bhamjee:** Writing – review & editing, Supervision, Software, Resources, Project administration, Methodology, Conceptualization. **Neil Martinson:** Writing – review & editing, Supervision, Resources, Methodology, Data curation, Conceptualization. **Simon Connell:** Writing – review & editing, Supervision, Software, Resources, Project administration, Methodology, Conceptualization.

Declaration of competing interest

The authors declare that they have no known competing financial interests or personal relationships that could have appeared to influence the work reported in this paper.

Acknowledgements

The authors extend their sincere appreciation to Clement Kleinstreuer and Sriram Vasudevan Chari from the Department of Mechanical Engineering at North Carolina State University for supplying the lung geometry, and the Department of Health Science at the University of Johannesburg and Professor Christopher Stein for their ongoing assistance with annual ethics approvals. Additionally, the authors are grateful to the Perinatal HIV Research Unit for providing the lung recordings and acknowledge the Centre for High Performance Computing (CHPC), South Africa, for providing computational resources to this research project. The opinions and conclusions expressed in this manuscript are exclusively those of the authors and do not represent the views of the University of Johannesburg, the Perinatal HIV Research Unit, the CHPC, or North Carolina State University.

Abbreviations

.aac	Advanced Audio Coding
AI	Artificial Intelligence
ANSYS	Analysis Systems Incorporation
BNS	Broadband Noise Source
CAP	Community-Acquired Pneumonia
CFD	Computational Fluid Dynamics
CFL	Courant–Friedrichs–Lewy
dB	Decibel
Exp	Experiment/Experimental (data)
FFT	Fast Fourier Transform
FSI	Fluid Structure Interaction
FW-H	Ffowcs Williams and Hawkings
GCI	Grid Convergence Index
Hosp-CAP	Hospitalized Community-Acquired Pneumonia
LES	Large Eddy Simulation
PEFR	Peak Expiratory Flow Rate
PHRU	Perinatal HIV Research Unit
RANS	Reynolds Averaged Navier–Stokes
SIMPLE	Semi-Implicit Method for Pressure Linked Equations
SPL	Sound Pressure Level
TB	Tuberculosis
URANS	Unsteady Reynolds Averaged Navier–Stokes
WALE	Wall-Adaptive Local Eddy
wav	Waveform

Nomenclature

a	Local speed of sound (m/s)
d	Diameter; d_p, D_p particle diameter (m)
$\bar{f}_i$	Mean body force
f_1, f_2, f_3	Performance parameter
$\vec{F}$	Force vector (N)
$\vec{g}$	Gravitational acceleration (m/s^2); standard value = 9.80665 m/s^2
k	Turbulent kinetic energy
k	Kinetic energy per unit mass (J/kg)
k, k_c	Mass transfer coefficient (units vary); also K, K_c
l, L	Length scale (m, cm)
L_I	Sound Intensity Level (dB)
m	Mass (g, kg)
M	Mach number (dimensionless)
p	Pressure (Pa, atm, mm Hg)
$\bar{p}$	Mean pressure
$\bar{\rho}$	Fluid density
$\overline{\rho u_i}$	Mean momentum flux
P_A	Acoustic power per unit volume of isotropic turbulence (W/m^3)
P_k	Production term for turbulence kinetic energy
P_{ref}	Reference Acoustic Power (W/m^3)
r	Radius (m); refinement ratio
Re	Reynolds number (dimensionless)
$S_{i,j}$	Mean rate-of-strain tensor (s^{-1})
t	Time (s)
u	Turbulence velocity
$\bar{u}_i$	Mean velocity component
$\overline{u_i u_j}$	Components of Reynolds stress tensor
$\overline{u_i' u_j'}$	Components of fluctuating velocity tensor
V	Volume (m^3)
$\vec{v}$	Overall velocity vector (m/s)
α	Volume fraction (dimensionless)
Δ	Change in variable (final - initial)
δ	Delta function (units vary)
δ_{ij}	Kronecker delta
ϵ	Turbulent dissipation rate (m^2/s^3)
η	Effectiveness factor (dimensionless)
μ	Dynamic viscosity (cP, Pa-s)
μ_t	Turbulent viscosity (realizable $k-\epsilon$ model)
υ	Kinematic viscosity (m^2/s)
ρ	Density (kg/m^3)
σ_k	Turbulent Prandtl number for k
σ_ϵ	Turbulent Prandtl number for ϵ
χ^2	χ^2 statistic
χ^2_{red}	Reduced χ^2 statistic
w	Specific dissipation rate (s^{-1})

Data availability

The data that has been used is confidential.

References

[1] G.E. Erhabor, Respiratory health in Africa: Strides and challenges, J. Pan Afr. Thorac. Soc. 2 (1) (2020) 11–17.

[2] J. Lee, et al., Extracellular vesicles as mediators of acute and chronic lung inflammation, Am. J. Physiol.-Lung Cell. Mol. Physiol. 322 (3) (2022) L495–L506.

[3] M. McIlwaine, J. Bradley, J.S. Elborn, F. Moran, Personalising airway clearance in chronic lung disease, Eur. Respir. Rev. 26 (143) (2017) 160086.

[4] E. Crame, M. Shields, P. McCrossan, Paediatric pneumonia: A guide to diagnosis, investigation and treatment, Paediatr. Child Health 31 (6) (2021) 250–257.

[5] M. Urbanowski, A. Ordonez, C. Ruiz-Bedoya, S. Jain, W. Bishai, Cavitary tuberculosis: The gateway of disease transmission, Lancet Infect. Dis. 20 (6) (2020) 117–128.

[6] H.R. Roberts, et al., Airflow obstruction in bronchiectasis: Correlation between computed tomography features and pulmonary function tests, Thorax 55 (3) (2000) 198–204.

[7] W.M. Faizal, et al., Computational fluid dynamics modelling of human upper airway: A review, Comput. Methods Programs Biomed. 196 (2020) 105627.

[8] A. Bohadana, G. Izbicki, S.S. Kraman, Fundamentals of lung auscultation, N. Engl. J. Med. 370 (8) (2014) 744–751.

[9] M. Sarkar, I. Madabhavi, N. Niranjan, M. Dogra, Auscultation of the respiratory system, Ann. Thorac. Med. 10 (3) (2015) 158–168.

[10] Reshmarani, N. Shilpa, H.C. Veena, Peak flow meter and digital spirometer: A comparative study of peak expiratory flow rate values, Natl. J. Physiol. Pharm. Pharmacol. 10 (6) (2020) 508–510.

[11] R. Sitalakshmi, K.N. Poornima, N. Karthick, The peak expiratory flow rate (PEFR): The effect of stress in a geriatric population of Chennai - A pilot study, J. Clin. Diagn. Res. 7 (2) (2013) 2728–2731.

[12] A. Oliveira, A. Marques, Respiratory sounds in healthy people: A systematic review, Respir. Med. 108 (4) (2014) 550–570.

[13] I. Katz, M. Pichelin, S. Montesantos, A. Murdock, S. Fromont, J. Venegas, G. Caillibotte, The influence of lung volume during imaging on CFD within realistic airway models, Aerosol Sci. Technol. 51 (2) (2017) 214–223.

[14] H.F. Chan, M.H. Tawhai, D.L. Levin, B.B. Bartholmai, A.R. Clark, Supine to upright lung mechanics: Do changes in lung shape influence lung tissue deformation? in: Proc. 36th Annu. Int. Conf. IEEE Eng. Med. Biol. Soc., 2014, pp. 832–835.

[15] W.-C. Su, Y.S. Cheng, Fiber deposition pattern in two human respiratory tract replicas, Inhal. Toxicol. 18 (10) (2006) 749–760.

[16] K.M. Makhanya, S. Connell, M. Bhamjee, N. Martinson, The use of computational fluid dynamics for assessing flow-induced acoustics to diagnose lung conditions, Math. Comput. Appl. 28 (3) (2023) 64.

[17] E. Andrès, R. Gass, A. Charloux, C. Brandt, A. Hentzler, Respiratory sound analysis in the era of evidence-based medicine and the world of medicine 2.0, J. Med. Life 11 (2) (2018) 89–106.

[18] A.H. Sfayyih, A.H. Sabry, S.M. Jameel, N. Sulaiman, S.M. Raafat, A.J. Humaidi, Y.M.A. Kubaiaisi, Acoustic-based deep learning architectures for lung disease diagnosis: A comprehensive overview, Diagnostics 13 (10) (2023) 1748.

[19] P.J. Roache, Perspective: A method for uniform reporting of grid refinement studies, J. Fluids Eng. 116 (3) (1994) 405–413.

[20] V.K. Srivastav, A.R. Paul, A. Jain, Capturing the wall turbulence in CFD simulation of human respiratory tract, Math. Comput. Simulation 160 (2019) 23–38.

[21] X. Luo, J. Hinton, T. Liew, K. Tan, LES modelling of flow in a simple airway mode, Med. Eng. Phys. 26 (2004) 403–413.

[22] ANSYS Inc., ANSYS Fluent Theory Guide, Release 2021R2 Edition, Canonsburg, PA, USA, 2021, Available from: https://www.ansys.com/products/fluids/ansys-fluent.

[23] L.F. Richardson, The generation of noise by isotropic turbulence, Proc. R. Soc. A 214 (1116) (1952) 119–132.

[24] F. Farassat, K.S. Brentner, The acoustic analogy and the prediction of the noise of rotating blades, Theor. Comput. Fluid Dyn. 10 (1–4) (1998) 155–170.

[25] M.E. Goldstein, An exact form of Lilley's equation with a velocity quadrupole/temperature dipole source term, J. Fluid Mech. 443 (2001) 231–236.

[26] AltairEngineering, Altair AcuSolve, version 2024.1, 2025, https://www.altair.com/altair-acusolve/, (Accessed 1 March 2025).

[27] H. Li, X. Li, J. Feng, Numerical study on normal lung sounds in bronchial airways under different breathing intensities, Biomed. Signal Process. Control. 86 (2024) 105053.

[28] A. Baranwal, D.A. Donzis, R.D.W. Bowersox, Asymptotic behaviour at the wall in compressible turbulent channels, J. Fluid Mech. 933 (2022) A28.

[29] Ansys, Inc., ANSYS Fluent, Release 2021R2, Ansys, Inc., Canonsburg, PA, USA, 2021, Available: https://www.ansys.com/products/academic/ansys-academic-research.

[30] M. Lasota, P. Šidlof, M. Kaltenbacher, S. Schoder, Impact of the sub-grid scale turbulence model in aeroacoustic simulation of human voice, Appl. Sci. 11 (4) (2021) 1970.

[31] M. Döllinger, C. Sittel, S. Kniesburges, C. Bohr, Computational fluid dynamics of upper airway aerodynamics during exercise: A patient-specific approach, Comput. Methods Biomech. Biomed. Eng. 26 (8) (2023) 873–886.

[32] Y. Mohamady, et al., Computational fluid dynamics of small airway disease in chronic obstructive pulmonary disease, EBioMedicine 114 (2025) 105670.

[33] D.J. Jasim, M.H. Chyad, Simulation of the turbulent air flow of inhalation and exhalation in the human respiratory system, Int. J. Thermofluids 26 (10) (2025) 101139.

[34] T. Gemci, et al., Computational model of airflow in upper 17 generations of human respiratory tract, J. Biomech. 41 (9) (2008) 2047–2054.

[35] L. Rochefort, et al., In vitro validation of computational fluid dynamic simulation in human proximal airways with hyperpolarized 3 He magnetic resonance phase-contrast velocimetry, J. Appl. Physiol. 102 (5) (2007) 2012–2023.

[36] M.H. Tawhai, E.A. Hoffman, C. Lin, The lung physiome: Merging imaging-based measures with predictive computational models, WIREs Syst. Biol. Med. 1 (1) (2009) 61–72.
[37] AudacityTeam, Audacity®, version 3.4.2, 2023, https://www.audacityteam.org/, (Accessed 2 June 2025).
[38] F. Nabeemeeah, et al., Cohort profile: the potentially preventable burden of community-acquired pneumonia in South African adults in the era of widespread PCV13 immunisation and antiretroviral therapy roll-out, before and during the COVID-19 pandemic - the multicentre, multimethod PotPrev study, BMJ Open 14 (12) (2024) e080553.
[39] M.J. Niedźwiecki, M. Ciołek, A. Gańcza, P. Kaczmarek, Application of regularized Savitzky–Golay filters to identification of time-varying systems, Automatica 133 (2021) 109865.
[40] CloudConvert, CloudConvert AAC to WAV converter, version 2.3, 2025, https://cloudconvert.com/aac-to-wav, (Accessed 2 June 2025).
[41] A.V. Hirtum, D. Berckmans, Assessing the sound of cough towards vocality, Med. Eng. Phys. 24 (7) (2002) 535–540.
[42] C.L. Lortie, M. Thibeault, M.J. Guitton, F. Champoux, Effects of age on the amplitude, frequency and perceived quality of voice, AGE 37 (6) (2015) 117.
[43] M. Abramowitz, I.A. Stegun (Eds.), Handbook of Mathematical Functions with Formulas, Graphs, and Mathematical Tables, in: National Bureau of Standards Applied Mathematics Series, vol. 55, U.S. Government Printing Office, Washington, D.C., ISBN: 978-0-486-61272-0, 1964.
[44] F. Andrani, M. Aiello, G. Bertorelli, E. Crisafulli, A. Chetta, Cough, a vital reflex. Mechanisms, determinants and measurements, Acta Biomed. 89 (4) (2019) 477–480.
[45] K.S. Hu, T.I.P. Shih, Large-eddy vs. Reynolds-averaged Navier–Stokes simulations of flow and heat transfer in a U-Duct with unsteady flow separation, Energies 17 (10) (2024) 2414.
[46] J. Pleil, M. Wallace, D. Wallace, M. Davis, C. Matty, The physics of human breathing: Flow, timing, volume, and pressure parameters for normal, on-demand, and ventilator respiration, J. Breath Res. 15 (4) (2021) 042002.
[47] C. Walsh, J. Brunet, D. Stansby, G. Gaisné, Y. Zhou, M. Ackermann, A. Bellier, C. Berruyer, A. Bocciarelli, M. Bodin, B. de Bakker, H. Dejea, A. De Maria Antolinos, K. Engel, A. Götz, J. Jacob, D. Jonigk, J. Purzycka, T. Urban, S. Verleden, R. Xue, P. Tafforeau, P. Lee, The human organ atlas, 2025, http://dx.doi.org/10.1101/2025.07.31.667856, BioRxiv Preprint, not peer-reviewed. Available under CC-BY-NC 4.0 license. URL https://www.biorxiv.org/content/10.1101/2025.07.31.667856v1.
[48] R. Xian, C. Walsh, S. Verleden, W. Wagner, A. Bellier, S. Marussi, M. Ackermann, D. Jonigk, J. Jacob, P. Lee, P. Tafforeau, A multiscale X-ray phase-contrast tomography dataset of a whole human left lung, Sci. Data 9 (1) (2022) 264, http://dx.doi.org/10.1038/s41597-022-01353-y.